A powerful (and likely young) radio-loud quasar at z=5.3

S. Belladitta[1,2], A. Moretti[1], A. Caccianiga[1], D. Dallacasa[3,4], C. Spingola[4], M. Pedani[5], L. P. Cassarà[6], and S. Bisogni[6]

1. INAF – Osservatorio Astronomico di Brera, via Brera, 28, 20121 Milano, Italy
   e-mail: silvia.belladitta@inaf.it
2. DiSAT, Università degli Studi dell'Insubria, Via Valleggio 11, 22100 Como, Italy
3. Dipartimento di Fisica e Astronomia, Università degli Studi di Bologna, Via Gobetti 93/2, I–40129 Bologna, Italy
4. INAF – Istituto di Radioastronomia, Via Gobetti 101, I–40129, Bologna, Italy
5. INAF – Fundación Galileo Galilei, Rambla José Ana Fernandez Pérez 7, 38712 Breña Baja, TF, Spain
6. INAF – Istituto di Astrofisica Spaziale e Fisica Cosmica (IASF), Via A. Corti 12, 20133 Milano, Italy

ABSTRACT

We present the discovery of PSO J191.05696+86.43172 (hereafter PSO J191+86), a new powerful radio-loud quasar (QSO) in the early Universe (z = 5.32). We discovered it by cross-matching the NRAO VLA Sky Survey (NVSS) radio catalog at 1.4 GHz with the first data release of the Panoramic Survey Telescope and Rapid Response System (Pan-STARRS PS1) in the optical. With a NVSS flux density of 74.2 mJy, PSO J191+86 is one of the brightest radio QSO discovered at z~5. The intensity of its radio emission is also confirmed by the very high value of radio loudness (R>300). The observed radio spectrum of PSO J191+86 shows a possible turnover around ~1 GHz (i.e., ~6 GHz in the rest frame), making it a Gigahertz-Peaked Spectrum (GPS) source. However, variability could affect the real shape of the radio spectrum, since the data in hand have been taken ~25 years apart. By assuming a peak of the observed radio spectrum between 1 and 2 GHz (i.e. ~ 6 and 13 GHz in the rest-frame) we found a linear size of the source of ~10-30 pc and a corresponding kinetic age of 150-460 yr. This would make PSO J191+86 a newly born radio source. However, the large X–ray luminosity (5.3×10^{45} erg s^{-1}), the flat X–ray photon index (Γ_X=1.32) and the optical-X–ray spectral index (α_{ox}=1.329) are typical of blazars. This could indicate that the non-thermal emission of PSO J191+86 is Doppler boosted. Further radio observations (both on arcsec and parsec scales) are necessary to better investigate the nature of this powerful radio QSO.

Key words. galaxies: active – galaxies: high-redshift – galaxies: jets – quasars: supermassive black holes - quasars: individual: PSO J191.05696+86.43172

1. Introduction

Radio-loud (RL) active galactic nuclei (AGN) are those supermassive black holes (SMBHs) that are able to expell part of the accreting matter into two relativistic bipolar jets (e.g., see Blandford et al. 2019 for a recent review). Therefore they are usually called *jetted* AGN (e.g., Padovani 2017) and they represent up to 10% of the total AGN population (e.g., Liu et al. 2021). Understanding the mechanisms responsible for the launch and the emission of these jets is of crucial importance to study their role in SMBHs accretion and evolution (e.g., Volonteri et al. 2015), as well as to investigate their feedback on the intergalactic medium (e.g., Fabian 2012).

High-redshift RL quasars (QSOs) are critical tools for studying the early evolutionary stage of the first jetted SMBHs, their feedback on the host galaxy and the environment, and their contribution to the re-ionization epoch (e.g., Blandford et al. 2019).

Among the more than 500 QSOs discovered to date at z>5, ~30 are classified as RL[1] (e.g., Romani et al. 2004; McGreer et al. 2006; Zeimann et al. 2011; Sbarrato et al. 2012; Bañados et al. 2018, 2021). Therefore, a systematic search and study of these objects is necessary to better constrain the properties of jetted SMBHs in the first Gyrs since the Big Bang.

In an effort to enlarge the current sample of high-z RL QSO,

we are conducting a project that combines optical, infrared, and radio datasets to identify distant radio sources all over the sky (Caccianiga et al. 2019, Belladitta et al. 2019, 2020, Ighina et al. in prep.). In this paper we present the discovery and the first observations of PSO J191.05696+86.43172 (hereafter PSO J191+86), a powerful jetted QSOs at z=5.3, which has been selected from the cross-correlation of the NRAO VLA Sky Survey (NVSS, Condon et al. 1998) in the radio, the Panoramic Survey Telescope and Rapid Response System (Pan-STARRS PS1, Chambers et al. 2016) in the optical and the AllWISE Source Catalog (Wright et al. 2010; Mainzer et al. 2011) in the mid-infrared (MIR).

The paper is organized as follows: in Sect. 2 the selection method is outlined; in Sect. 3 new optical and near-infrared (NIR) spectroscopic observations of PSO J191+86 are presented; in Sect. 4 and Sect. 5 archival radio data and a new X-ray follow-up observation are reported, respectively; the results on the multiwavelength properties of the source are described in Sect. 6 and 7; finally Sect. 8 reports a brief discussion and conclusions.

The magnitudes used in this work are all in the AB system, unless otherwise specified. We use a flat Λ cold dark matter (ΛCDM) cosmology with H_0 = 70 km s^{-1} Mpc^{-1}, Ω_m = 0.3 and Ω_Λ = 0.7. Spectral indices are given assuming $S_\nu \propto \nu^{-\alpha}$ and all errors are reported at 1σ, unless otherwise specified. Throughout the paper the flux densities are the observed ones, while luminosities are given in the source's rest-frame, unless otherwise specified.

---

[1] Usually an AGN is considered to be radio loud when it has a radio loudness R>10, with R defined as the ratio of the 5 GHz and 4400Å rest-frame flux densities: R = $S_{5\text{GHz}}$ /$S_{4400\text{Å}}$ (Kellermann et al. 1989).

2. Source selection

From the entire NVSS catalog, we selected bright ($S_{1.4GHz} \geq 30$ mJy) and compact objects to provide an accurate ($<2''$) radio position. With this criteria we found ~45000 sources. We then cross-matched them with the Pan-STARRS PS1 catalog, using a maximum separation equal to $2''$. This impact parameter guarantees to recover more than 90% of the real optical counterparts (Condon et al. 1998). We selected only relatively bright optical sources ($i_{PS1} < 21.5$) outside the Galactic plane ($|b| \geq 20°$), to minimize contamination from stars, and at Dec>-25°, to exclude optical objects at the declination limit of Pan-STARRS survey. Then all the sources that satisfied the following photometric criteria have been selected:
i) no detection in g_{PS1}-band;
ii) drop-out: r_{PS1}-$i_{PS1} \geq 1.2$;
iii) blue continuum: i_{PS1}-$z_{PS1} \leq 0.5$;
iv) point-like sources: i_{PS1}-$i_{Kron} < 0.05$;
v) no detection in WISE (W2) or i_{PS1} - W2(Vega) < 5.0.
This last constraint has been placed to minimize the contamination by dust reddened AGN at z = 1-2 (e.g., Carnall et al. 2015; Caccianiga et al. 2019).

Fourteen candidates remained after the application of these filters; four of them are already known radio QSOs in the literature. PSO J191+86 stands out among the other 10 targets for its very high value of the drop-out ($r - i > 1.7$), its photometric redshift (z>5) and its very high radio flux density ($S_{1.4GHz} > 70$ mJy). Therefore we considered only this source for a spectroscopic follow-up.

In Table 1 the Pan-STARRS PS1 and WISE magnitudes of PSO J191+86 (corrected for Galactic extinction, using the extinction law provided by Fitzpatrick (1999), with $R_V = 3.1$) are reported. Figure 1 shows the optical images of the source in the different g, r, i, z, y PS1 bands. The optical coordinates of PSO J191+86 are: R.A. = 191.05696 deg ($12^h44^m13.902^s$), Dec = +86.43172 deg ($+86^d25'54.07''$).

Table 1: Optical and MIR magnitudes of PSO J191+86.

filter	central λ	mag	Ref. survey
	(μm)	(AB)	
(1)	(2)	(3)	(4)
r_{PS1}	0.680	21.34 ± 0.15	PS1
i_{PS1}	0.745	19.78 ± 0.04	PS1
z_{PS1}	0.870	19.49 ± 0.03	PS1
y_{PS1}	0.978	19.22 ± 0.06	PS1
$W1$	3.4	18.502 ± 0.035	WISE
$W2$	4.6	18.386 ± 0.051	WISE

Notes. Col (1): optical / MIR filters; Col (2): filter central wavelength in μm; Col (3): observed AB de-reddened magnitude; Col (4): reference catalog. The offset between the Pan-STARRS PS1 optical and WISE MIR positions is $0.85''$. The relations to convert from Vega to AB systems are: $W1_{AB} = W1+2.683$; $W2_{AB} = W2+3.319$ (Cutri et al. 2012).

3. Optical, NIR observations and data reduction

3.1. TNG/DOLORES observation

We performed a dedicated spectroscopic follow-up of PSO J191+86 with DOLORES (Device Optimized for the LOw RESolution) installed at the Telescopio Nazionale Galileo (TNG). We confirmed PSO J191+86 as a high-z RL QSO the night of the 21 June 2018, with a single 30 minutes observation

Table 2: Summary of the Optical and Near-infrared Follow-up Spectroscopic Observations of PSO J191+86.

Date	Telescope/Instrument	Exposure Time	S/N
(1)	(2)	(3)	(4)
2018 June 21	TNG/DOLORES	0.5h	~7
2019 May 3	LBT/LUCI1	1.8h	~7.5
2019 May 3	LBT/LUCI2	1.8h	~7.5

Notes. Col(1): Date of the observation; Col(2): Telescope and instrument used; Col(3): Totale exposure time; Col(4): Signal-to-noise ratio of the continuum.

with the LR-R grism and a long-slit of $1''$ width. The mean air mass during the observation was 1.7. Table 2 reports the details of this observation.

An exposure of a Ar+Ne+Hg+Kr lamp was done to ensure the wavelength calibration and the flux calibration was obtained by observing the G191-B2B (R.A.=$05^h05^m30.62^s$, Dec=$+52^d49'54.0''$) spectro-photometric standard star of the catalogs of Oke (1990).

The data reduction was performed using standard Image Reduction and Analysis Facility (IRAF) procedures (Tody 1993). The DOLORES discovery spectrum is shown in Fig. 2; it has been corrected for Galactic extinction as explained in Sect. 2.

3.2. LBT/LUCI follow-up

We performed a spectroscopic follow-up with LBT utility camera in the infrared (LUCI, Seifert et al. 2003) at the Large Binocular Telescope (LBT) in order to extend the wavelength range in the NIR band and detect the CIVλ1549 (hereafter CIV) and the MgIIλ2798 (hereafter MgII) broad emission lines (BELs), which can be used to estimate the central black hole mass of PSO J191+86 thanks to the so-called single epoch (SE) or virial method (e.g., Vestergaard & Peterson 2006, hereafter VP06, see Sect. 6.1). The observation was carried out on the night of 2019 May 3 (P.I. Moretti A., program ID: LBT2018AC123500-1) and consisted of 12 exposures of 270s each in nodding mode in the sequence ABBA, with a total integration time of 1.8 hours. The medium seeing along the night was $0.9''$ and the mean air mass was 1.7. The details of this observation are reported in Table 2. We decided to use the grism 200 with the zJ and HK filters on LUCI1 and LUCI2 respectively in order to cover all the spectral range and detecting the CIV (LUCI1) and the MgII (LUCI2) simultaneously. The G200-zJ configuration allowed us to observe the wavelength range from 0.9 to 1.2 μm, where the CIV line is expected (λ_{obs} = 9805Å at z=5.3); instead the G200-HK configuration covers the range from 1.5 to 2.4 μm in which the MgII line falls (expected λ_{obs} = 17700Å). The data reduction was performed at the Italian LBT Spectroscopic Reduction Center, with the software developed for LBT spectroscopic data reduction (Gargiulo et al. 2022). Each spectral image was independently dark subtracted and flat-field corrected. Sky subtraction was done on 2D extracted, wavelength calibrated spectra. Wavelength calibration was obtained by using several sky lines, reaching a rms of 0.25Å on LUCI1 and 0.5Å on LUCI2.

In Fig. 2 we report the LBT/LUCI1 and the LBT/LUCI2 spectra in which the CIV and the MgII BELs have been detected, together with the CIII]λ1909+AlIIIλ1860+SiIII]λ1892 complex. Also in this case, the two spectra have been corrected for Galactic extinction as the TNG/DOLORES one. We note that the MgII line suffers from the presence of an absorption feature (a resid-
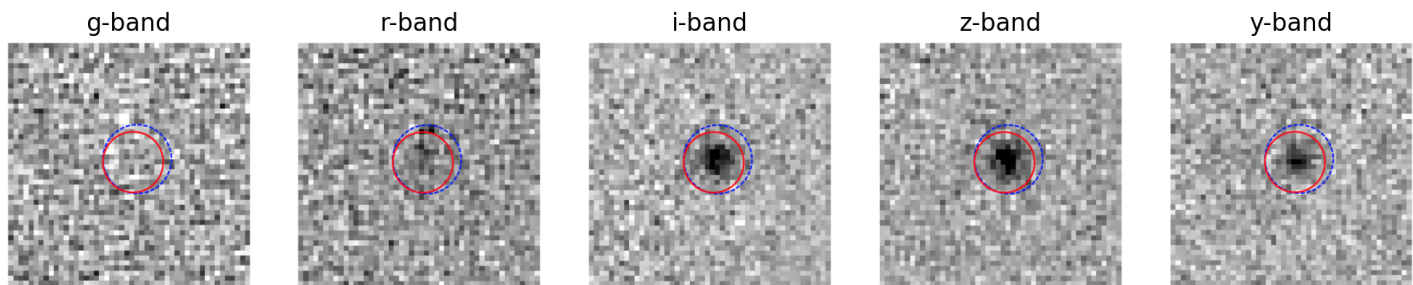
g-band	r-band	i-band	z-band	y-band

Fig. 1: 0.2′×0.2′ Pan-STARRS PS1 g, r, i, z, y cutout images of PSO J191+86. Its optical position is marked with a red circle of 1.5″ of diameter. The radio NVSS position is marked with a blue dashed circle, as large as the radio positional error reported in the catalog (1.7″). All images are oriented with north up and east to the left.
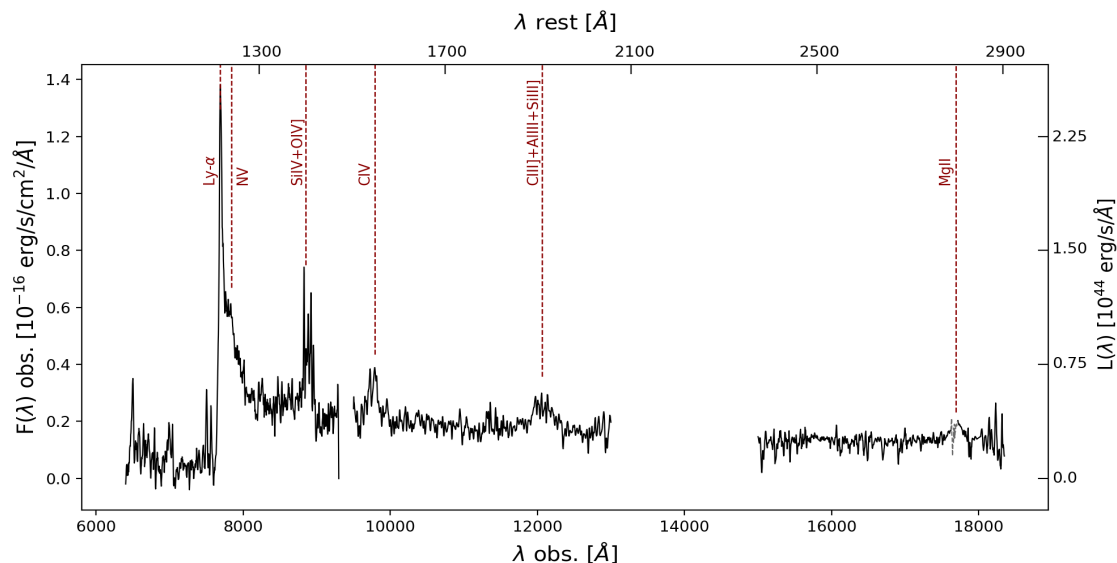

Fig. 2: Optical and NIR de-reddened observed spectra of PSO J191+86 taken at TNG and LBT respectively. The most important visible emission lines are marked. In grey we mask the part of the MgII line that suffers from a strong absorption feature, in which the peak of the MgII line falls. **The top x-axis reports the rest-frame wavelengths while the right axis shows the monochromatic luminosity.**

ual of background subtraction, see grey line in Fig. 2 and the zoom-in in Fig. 6). When masking the absorption feature, the wide range of absorption results in a gap close to the line center.

4. Archival continuum radio data

Beside the NVSS observation at 1.4 GHz ($S_{1.4GHz}$=74.2±2.3 mJy, see also Fig. 3), PSO J191+86 has an archival detection also in the Westerbork Northern Sky Survey (WENSS, Rengelink et al. 1997, see Fig. 3) at 325 MHz of 19.0±3.3 mJy. Because of these two flux densities, Massaro et al. (2014) included PSO J191+86 in the LOw frequency Radio CATalog of flat spectrum sources (LORCAT). Moreover the source was observed by Healey et al. (2009) at 4.85 GHz with the Effelsberg 100 m telescope. The authors measured a flux density of 33.7±1.3 mJy. The detections with WENSS, NVSS and Effelsberg enabled Healey et al. (2009) to classify PSO J191+86 as a Gigahertz-Peaked Spectrum (GPS) source, meaning a young ($<10^{3-4}$yr) and compact (<1 kpc) radio source. They are usually considered an early stage evolution of powerful large-scale radio galaxies of the local Universe (see O'Dea & Saikia 2021 for a recent review). PSO J191+86 is also clearly detected at 3 GHz in the Very Large Array Sky Survey (VLASS, Lacy et al. 2020, see Fig. 3 and Fig. 4). The source has been observed both during the first campaign

of the first epoch (VLASS 1.1) in 2017 and the first campaign of the second epoch (VLASS 2.1) in 2020. Since the data of the 1.1 epoch suffers from phase errors, i.e. artifacts that alter the true size and morphology of a source, we carried out the analysis only on the 2.1 image. We performed a single Gaussian fit, by using the task IMFIT of the Common Astronomy Software Applications package (CASA, McMullin et al. 2007) to quantify the flux density and the size of PSO J191+86 (see Fig. 4). The measurements of total and peak flux densities and sizes obtained from the best fit are listed in Table 3. The position of the source estimated by the fit is: RA = $12^h44^m13.57949^s \pm 0.01239^s$, Dec = $+86^d25'54.04861'' \pm 0.00021^s$, that is at 0.3″ from the optical PS1 position, confirming the radio-optical association of PSO J191+86. By comparing the dimension of the source as estimated by the single Gaussian fit with the beam size (major axis = 4.372″, minor axis = 2.241″, P.A. = 80.75 deg, East of North), we concluded that the source is partially resolved.

Finally PSO J191+86 is not detected in the TIFR GMRT Sky Survey (TGSS, Intema et al. 2017) at 150 MHz. From the TGSS image we computed only an upper limit (at 2σ) of ∼4 mJy.

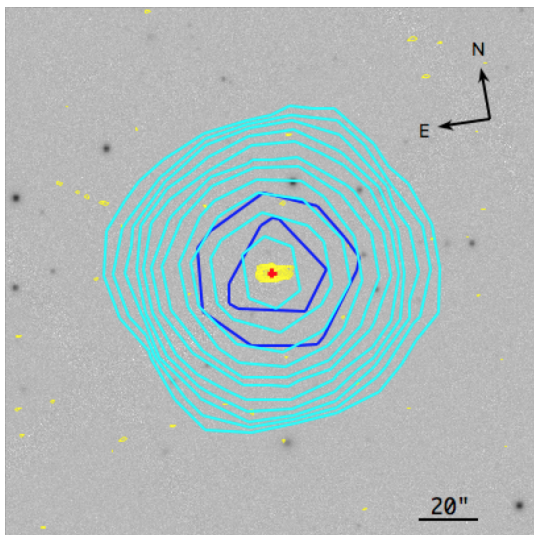In Table 4 all the available radio flux densities of PSO J191+86

Fig. 3: $3' \times 3'$ cutout of the i_{PS1} image around PSO J191+86 overlaid with the radio contours from NVSS (1.4 GHz, cyan), WENSS (325 MHz, blue) and VLASS (3 GHz, yellow). In all the cases contours are spaced by $\sqrt{2}$ starting from three times the survey RMS (NVSS = 0.42 mJy beam^{-1}; VLASS = 160 μJy beam^{-1}; WENSS = 2.7 mJy beam^{-1}). A zoom-in on the VLASS emission is shown in Fig. 4. The red cross indicates the optical position of the source.

are reported. The VLASS integrated flux density has been corrected for the 3% of systematic uncertainty[2].
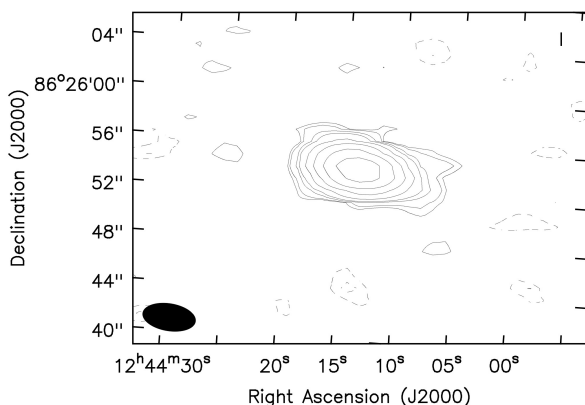
Fig. 4: VLASS 2.1 image of PSO J191+86. The contours are drawn at $(-3, -2, 2, 3, 6, 9, 18, 36, 72,$ and $144)$ times the off-source RMS (160 μJy). In the bottom left corner the beam size ($4.372'' \times 2.241''$) is shown. North is up, east is left.

5. *Swift*-XRT follow-up

PSO J191+86 was observed in the X–rays by the *Swift*–XRT telescope (target ID: 3110833; P.I. Belladitta S.). The observations were carried out between September, October and November 2020 and consisted of 44 segments for a total exposure time of 47.81 ks. Data have been reduced through the standard data analysis pipeline (Evans et al. 2009), running on the UK *Swift* Science Data Centre web page[3] using HEASOFT v6.26.1.

---

[2] https://science.nrao.edu/vlass/data-access/vlass-epoch-1-quick-look-users-guide

[3] https://www.swift.ac.uk/index.php

The source is clearly detected with a total of 55 counts and with an expected background of 7 counts in [0.5-10] keV energy band. The standard (PSF-fitted) *Swift*–XRT position of the source, calculated by the detected and centroid algorithm is RA = $12^h 44^m 12.97^s$, Dec = $+86^d 25' 57''$, with an uncertainty of 3.5'' (90% confidence). This is at 3.0'' from the optical PS1 position. A standard spectral analysis has been performed using XSPEC (v.12.10.1) by fitting the observed spectrum (Fig. 5) with a single power law with the absorption factor fixed to the Galactic value (6.46×10^{20} cm^{-2}) as measured by the HI Galaxy map of Kalberla et al. (2005). We measured a photon index (Γ_X) of 1.32 ± 0.2, which implies an X–ray spectral index ($\alpha_x = \Gamma_X - 1$) of 0.32, and a flux of $8.11^{+1.63}_{-1.47} \times 10^{-14}$ erg s^{-1} cm^{-2} in the observed [0.5-10] keV energy band.
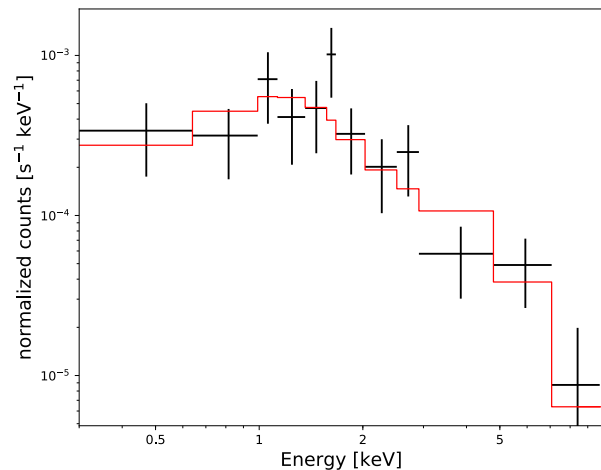

Fig. 5: *Swift*–XRT observed spectrum of PSO J191+86 modelled with a single power-law with only Galactic absorption (solid red line).

6. Analysis of MgII and CIV broad emission lines

Among all the emission lines detected in the TNG and LBT spectra, we focused on the CIV and MgII BELs; the latter allowed us to measure the redshift of the source and together with the CIV provides an estimation of the mass of the black hole hosted by PSO J191+86. To derive the properties of the two BELs (e.g., redshift, line width, line luminosity) we followed the approach of several works in the literature based on the analysis of high-z QSO spectra (e.g., Mazzucchelli et al. 2017; Schindler et al. 2020; Bañados et al. 2021; Vito et al. 2022; Farina et al. 2022). First, we subtracted to the spectra the continuum emission, described by a *power law ($f_{pl} \propto \lambda/2500\text{Å}^{\alpha_\lambda}$)*, an iron pseudo-continuum template and a Balmer pseudo-continuum. We modeled the Fe II contribution with the empirical template of Vestergaard & Wilkes (2001), which is used in the derivation of the scaling relation that we later consider for estimating the black hole mass of the QSO (see Sect. 6.1). To be consistent with previous literature works (e.g., Vito et al. 2022 and reference therein), with an iterative process, we convolved the iron pseudo-continuum model with a Gaussian function with the width being equal to that of the MgII emission line, since it is assumed that FeII emission arises from a region close to that responsible for the MgII emission. To perform the continuum fit, we chose a region of the quasar continuum free of broad emission lines and of strong spikes from residual atmospheric emission: [10520-11110]Å in the LUCI1 spectrum and [15979-17200]Å

Table 3: Properties of the quick look VLASS 2.1 image of PSO J191+86.

Obs. (Rest) Freq. (GHz)	Total flux density (mJy)	Peak surface brightness (mJy beam^{-1})	major axis (arcsec)	minor axis (arcsec)	P.A. (deg)
(1)	(2)	(3)	(4)	(5)	(6)
3.0 (18.96)	40.57±0.32	38.83±0.17	1.16±0.10	<0.39	75±7

Notes. Col(1): observing frequency (rest-frame frequency in parenthesis); Col(2): integrated flux density; Col(3): peak surface brightness; Col(4)-Col(5): de-convolved major and minor axes of the source estimated directly from the Gaussian fit; Col(6) position angle (east of north).

Table 4: Summary of the archival radio observations of PSO J191+86.

Obs. Freq. (GHz)	S_ν (mJy)	Survey or Follow-up	Resolution (arcsec)	Obs. date
(1)	(2)	(3)	(4)	(5)
0.150	< ~4^a	TGSS	25	15/03/2016
0.325	19.0±3.3	WENSS	15	15/06/1997
1.4	74.2±2.3	NVSS	45	24/06/1996
3.0	41.82±0.32	VLASS	2.5	30/08/2020
4.85	33.7±1.3	Effelsberg	150	June 2008

Notes. Col(1): Observed frequency in GHz; Col(2): integrated flux density in mJy; a: the TGSS value is an upper limit (at 2σ); Col(3): reference survey or dedicated follow-up; *Effelsberg* refers to the observation carried out by Healey et al. (2009) with the 100m Effelsberg telescope. Col(4): angular resolution in arcsec; Col(5): Date of the observation.

in the LUCI2 spectrum (see Fig. 6). We then subtracted the entire pseudo-continuum model from the observed spectra, and we modeled the two BELs with Gaussian functions.

BELs are usually well described by a multiple Gaussian profile (e.g., Marziani et al. 2010; Shen et al. 2011, 2019; Tang et al. 2012; Karouzos et al. 2015; Rakshit et al. 2020). In particular, we considered a model where each line is described by a broad plus a narrow component to account for a possible contribution from the Narrow Line Region. Each broad line is modelled with 1 or 2 Gaussians, while the narrow component is modelled with a Gaussian with FWHM below 1000 km s^{-1} and larger than the spectral resolution (FWHM>~200 km s^{-1}). In the case of MgII, we also considered that the line is a doublet (λ2796/2803) with an intensity ratio set equal to 1:1 (e.g., Marziani et al. 2013). For the MgII, we found that the narrow component is not statistically required and has no impact on the width of the broad component. The broad component of each line of the doublet is modelled with 2 Gaussian functions (hence 4 Gaussians in total for describing the entire line profile, see Fig. 6). Similarly, for the CIV we did not find a clear evidence of a narrow component. This is in agreement with several works in the literature, which report that the existence of a strong narrow component for CIV line is controversial (Wills et al. 1993; Corbin & Boroson 1996; Vestergaard 2002; Shen & Liu 2012). Instead, the broad component is well fitted with a single Gaussian (Fig. 6). On the right side of the CIV we also fitted with a single Gaussian profile the Heλ1640 emission line (see Fig. 6). The uncertainties on broad emission lines properties were evaluated through a Monte Carlo method (e.g., Raiteri et al. 2020; Zuo et al. 2020; Diana et al. 2022). Each wavelength of the best fit model was randomly perturbed for 1000 times, according to a Gaussian distribution of the mean rms of the spectra computed underneath the emission lines on the pseudo-continuum subtracted spectrum. In this way we obtained 1000 different mock spectra of the lines profiles, from which we measured the line properties with the same procedure

used on the real data. We computed the distributions of all the line properties for these 1000 simulated spectra, and the interval that contains 68% of the data in these distributions was taken as the statistical uncertainty on the best fit values. From the multi-Gaussian modelling we measured the following line parameters: redshift, line width (parameterized as the FWHM), rest-frame equivalent width (REW), line flux and luminosity (see Table 5). We adopted as the systemic redshift of PSO J191+86 the one derived from the MgII line, which is usually taken as the best redshift estimator for high-z objects when sub-mm and mm data are not available (e.g. De Rosa et al. 2014; Mazzucchelli et al. 2017; Schindler et al. 2020). We note that, despite the absorption feature in the middle, the redshift estimated by the MgII line is consistent with the expected positions of the Ly$_\alpha$ and NV lines (see right panel of Fig.6).

6.1. Estimates of the black hole mass

The most common method used to compute the mass of the central BH of Type I AGN is the SE method (e.g., Mazzucchelli et al. 2017; Shen et al. 2011; 2019; Diana et al. 2022). The underlying assumption of this technique is that the dynamics of the gas clouds is dominated by the central black hole gravitational potential. CIV and MgII BELs are usually the most used lines to compute the mass of the central SMBH hosted by high-z QSOs. However, several works have questioned the reliability of CIV as a good virial mass indicator (e.g., Sulentic et al. 2007; Trakhtenbrot & Netzer 2012; Bisogni et al. 2017; Marziani et al. 2019) due to its observed blueward asymmetry and velocity shifts of the line profile with respect to low ionization lines, independently from the source orientation (e.g., Gaskell 1982; Richards et al. 2011; Coatman et al. 2017; Runnoe et al. 2014; Zuo et al. 2020). These characteristics suggest that the CIV clouds are affected by non-gravitational effects, such as outflows, which have a significant effect on the observed emission velocity profile. The so-called weak emission line quasar population (WELQs, Diamond-Stanic et al. 2009, REW<10Å) exhibits the largest blueshift (>3000 km s^{-1}, see e.g., Vietri et al. 2018). With a REW of ~150Å, it is clear that PSO J191+86 does not belong to this QSO population and, therefore, we do not expect to find a high value of blueshift for our source. Moreover, several works in the literature (e.g., Marziani et al. 1996; Sulentic et al. 2007; Richards et al. 2011) claimed that RL sources usually show lower value of blueshfit with respect to radio quiet (RQ, or *non-jetted*) objects.

Other authors, instead, have demonstrated that there is a consistency between the SE M$_{BH}$ computed from CIV and Balmer lines (e.g., VP06; Greene et al. 2010; Assef et al. 2011; Dalla Bontà et al. 2020). Finally, Shen et al. (2019) report that CIV can still be used because on average it provides consistent black hole masses with those obtained from low ionization lines, albeit with a large intrinsic scatter. Therefore, we decided to compute the black hole mass also by using the CIV, even if we considered
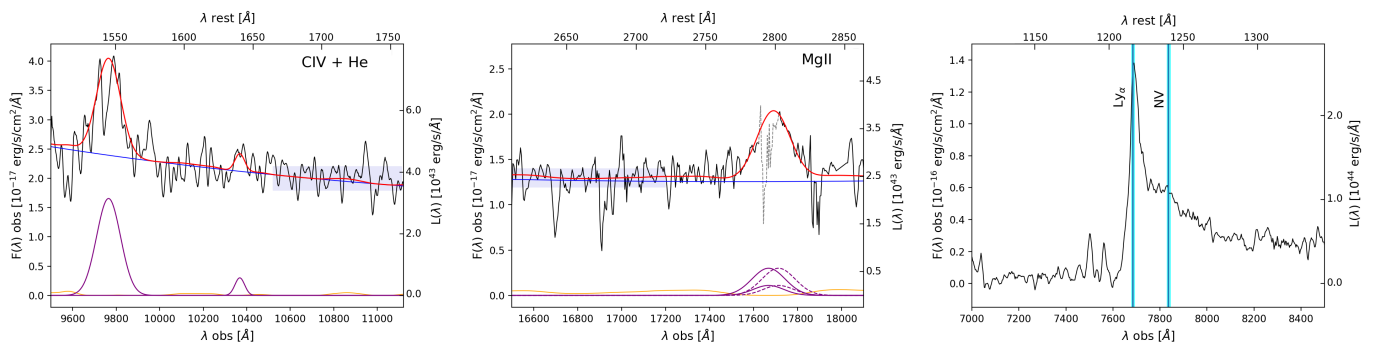
Fig. 6: Zoom-in on CIV and MgII lines fit and on the Ly$_\alpha$+NV region. *Left and central panel*: We show the total spectral fit (red line), and the different components, i.e., power law + Balmer pseudo-continuum (blue line), Fe II template (orange line, from Vestergaard & Wilkes 2001), and emission lines (purple). For the MgII we represent the two line of the doublet (solid Gaussians and dashed Gaussians respectively). Spectral regions used for the continuum fits are shown as horizontal light blue shaded areas. In the right panel, the absorption feature in the middle of the MgII line is masked (grey dotted line). *Right panel*: Ly$_\alpha$ and NV spectral region. The blue vertical lines represent the position of the two BELs based on the MgII line redshift. The cyan shaded region is the uncertainty on this redshift estimate. **The top x-axis reports the rest-frame wavelengths while the right axis shows the monochromatic luminosity.**

Table 5: Properties of CIV and MgII BELs.

Emission line	Redshift	FWHM km s^{-1}	REW Å	F$_{line}$ 10^{-15} erg s^{-1}cm^{-2}	L$_{line}$ 10^{44} erg s^{-1}	M$_{BH}$ 10^9M$_\odot$
(1)	(2)	(3)	(4)	(5)	(6)	(7)
CIV	5.304±0.011	3762^{+124}_{-166}	$149.75^{+5.26}_{-4.82}$	$2.26^{+0.11}_{-0.08}$	$6.49^{+0.26}_{-0.17}$	$2.40^{+0.42}_{-0.39}$
MgII	5.320±0.005	2968^{+339}_{-395}	$66.15^{+16.11}_{-13.12}$	$0.61^{+0.17}_{-0.19}$	$1.85^{+0.54}_{-0.56}$	$1.67^{+0.40}_{-0.46}$

Notes. Col (1): Emission line; Col (2): Redshift, estimated from the line peak; for the MgII we report the parameters of the single doublet line. The redshift of PSO J191+86 used throughout the paper is taken from the fit to the MgII BEL; Col (3): FWHM in km s^{-1}; Col (4): rest-frame equivalent width; Col (5) and (6): line flux and line luminosity; Col (7): SE black hole mass. Here we report the statistical uncertainty computed by propagating the error on the FWHM and continuum luminosity. In the total mass error the scaling relation scatter (0.55 dex for MgII and 0.36 dex for CIV) should be added.

as our best estimator the mass based on MgII.

For the MgII we used the SE scaling relation presented by Vestergaard & Osmer (2009), for a direct comparison with other estimates in the literature:

$$M_{BH} = 10^{6.86}\left[\frac{\text{FWHM (MgII)}}{1000 \text{ km/s}}\right]^2 \left[\frac{\lambda L_\lambda \text{ (3000Å)}}{10^{44} \text{ erg/s}}\right]^{0.5} \quad (1)$$

where $\lambda L_\lambda(3000\text{Å})$ is the monochromatic luminosity at 3000Å derived from the power-law model[4]: λL_λ (3000 Å) = $6.57\pm0.62\times10^{46}$ erg s^{-1}. We obtained a black hole mass of $1.67^{+4.18}_{-1.26}\times10^9M_\odot$. With respect to the uncertainty reported in Table 5, here the error on M$_{BH}$ already takes into account the intrinsic scatter of the scaling relation (0.55 dex) which is the dominant uncertainty of the black hole mass estimate. Consistent black hole mass estimates are obtained by using different scaling relations reported in the literature, both based on the continuum luminosity (e.g., McLure & Dunlop 2004; Shen & Liu 2012) and on the MgII line luminosity (e.g., Shen & Liu 2012).

For the CIV we used the scaling relation of VP06, the most used in the literature:

$$M_{BH} = 10^{6.66}\left[\frac{\text{FWHM (CIV)}}{1000 \text{ km/s}}\right]^2 \left[\frac{\lambda L_\lambda \text{ (1350Å)}}{10^{44} \text{ erg/s}}\right]^{0.53} \quad (2)$$

The continuum luminosity (λL_λ) at 1350Å has been directly estimated from the TNG rest frame spectrum: $6.78\pm0.97\times10^{46}$ erg s^{-1}. Before applying this scaling relation, we corrected the FWHM (CIV) value for blueshift effect, by following the prescription of Coatman et al. (2017):

$$\text{FWHM (CIV)\_corr} = \frac{\text{FWHM (CIV)}}{\alpha \times \frac{\Delta_v}{1000\text{km/s}} + \beta} \quad (3)$$

where α=0.41±0.02, β=0.62±0.04 and ΔV is the line blueshift defined as:

$$\Delta V(\text{km s}^{-1}) = c \times \frac{1549.48\text{Å} - \lambda_{\text{half}}}{1549.48\text{Å}} \quad (4)$$

where c is the speed of light, 1549.48Å is the rest frame wavelength for the CIV and λ_{half} is the line centroid[5]. We found a ΔV of 741^{+350}_{-424} km s^{-1}, which is small, as expected, and allowed us to infer that the virial black hole mass of PSO J191+86 based on CIV line should not be strongly affected by blueshift effects. A similar value of ΔV is found by using λ_{peak} (i.e., the peak of the CIV line obtained by the Gaussian model in Fig. 6) with respect to λ_{half}: 759±522 km s^{-1}.

The corrected FWHM (C IV) is 4072^{+180}_{-134} km s^{-1} and, hence, the M$_{BH}$ is equal to $2.40^{+3.11}_{-1.40}\times10^9M_\odot$. The reported error already

---

[4] Since the LUCI2 spectrum does not cover the wavelengths up to 3000Å, we used the continuum near the MgII line, between 2720Å and 2750Å, and extrapolate it to 3000Å using the power-law index estimated from our data (α_λ = -1.51).

[5] The line centroid is defined as the wavelength that bisect the line in two equal part. We used the definition of Dalla Bontà et al. (2020): λ_{half} = $\frac{\int \lambda P(\lambda) d\lambda}{\int P(\lambda) d\lambda}$, where P($\lambda$) is the line profile.

takes into consideration the intrinsic scatter of the used scaling relation (0.36 dex; VP06). By taking into account only the statistical uncertainty (see Table 5) the black hole mass derived from CIV is consistent within 1σ to the one estimated form the MgII line.

6.1.1. Bolometric luminosity and Eddington ratio

The value of M_{BH} allowed us to derived the Eddington ratio of the source, which quantify how fast is the black hole accreting with respect to the Eddington limit: $\lambda_{Edd} = \frac{L_{bol}}{L_{Edd}}$, where, L_{Edd} is the Eddington luminosity, the maximum luminosity beyond which radiation pressure will overcome gravity[6] and L_{bol} is the bolometric luminosity, i.e., the total energy produced by the AGN per unit of time integrated on all the wavelengths. To estimate it we used the continuum luminosity at 3000Å compute in the previous sub-section and the following bolometric correction: $L_{bol} = K \times L_{3000\text{Å}}$, where $K = 5.15 \pm 1.26$ (Shen et al. 2008). We obtained: $L_{bol}=3.38\pm1.14\times10^{47}$ erg s^{-1}. The corresponding value of λ_{Edd} is: $= 1.55^{+1.08\ (3.50)}_{0.95\ (-1.37)}$. The uncertainty in parenthesis takes into account both the statistical error on the virial mass and the intrinsic scatter of the SE relation.

The SE M_{BH} and of λ_{Edd} of PSO J191+86 are similar to those derived for RL and RQ QSOs discovered in the same range of redshift (z=4.5-5.5; e.g., Shen et al. 2011; Yi et al. (2014); Trakhtenbrot 2021; Diana et al. 2022). This similarity of masses and Eddington ratio could be likely a consequence of a selection bias, as all these high-z sources have been selected from similar optical/IR surveys.

7. Analysis of the radio and X–ray properties

7.1. Radio spectrum

From the radio flux densities listed in Table 4 we computed the radio spectral index of PSO J191+86. We found that the radio spectrum shows a peak around ~1 GHz (observed frame, Fig. 7, ~6.3 GHz in the source's rest frame). By assuming that the 1.4 GHz detection glimpses the turnover, we estimated the radio spectral indices below and above this potential peak and assuming a single power-law for the continuum emission ($S_\nu \propto \nu^{-\alpha}$). The spectral index between 325 MHz and 1.4 GHz ($\alpha^{1.4}_{0.325}$) is -0.93 ± 0.28 and $\alpha^{4.85}_{1.4}$ (the spectral index between 1.4 and 4.85 GHz) is 0.65 ± 0.12. Therefore PSO J191+86 can be classified as a GPS source, according to Healey et al. (2009).

Since the radio data in hand are not simultaneous (spanning over ~25 years), variability may be affecting the observed spectrum, making it to appear flat (e.g., Dallacasa 2000, Orienti & Dallacasa 2020). To date we have no information about possible flux density variability of the source. A nearly simultaneous sampling of the radio spectrum (in particular below the possible turnover) is necessary.

7.2. Radio-loudness

From the observed radio and optical flux densities we computed the radio-loudness (R) of PSO J191+86, which quantifies the level of power of the non-thermal synchrotron radio emission with respect to the thermal one originated in the accretion disk. It is defined as the ratio between the rest-frame radio (5 GHz) and optical (blue band B at 4400Å) fluxes (Kellerman et al. 1989): R

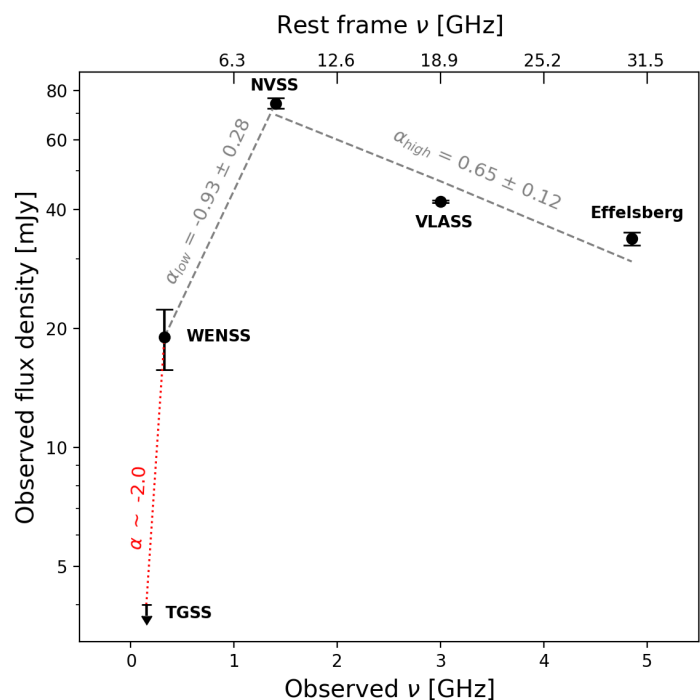[6] $L_{Edd} = 1.26 \frac{M_{BH}}{M_\odot} \times 10^{38}$ erg s^{-1}

Fig. 7: Radio flux densities as a function of the observed (bottom x-axis) and rest-frame (top x-axis) frequency of PSO J191+86 from 0.150 to 4.85 GHz. The spectrum shows a peak around ~1 GHz, hence the source can be classified as a GPS. The corresponding indices of the low and high frequency part of the spectrum are reported together with the reference surveys. The red dashed line represents the possible spectral index according to the TGSS upper limit.

$= \frac{S_{5\text{GHz}}}{S_{4400\text{Å}}}$. We estimated the flux density at 5 GHz by extrapolating the 1.4 GHz value adopting the spectral index of the optically thick part of the spectrum ($\alpha^{1.4}_{0.325}$). We highlight that 5 GHz in the rest-frame corresponds to 0.789 GHz in the observed frame. The value of the flux density at 4400Å rest frame was derived from the LUCI2 rest frame spectrum and assuming the optical spectral index of Vanden Berk et al. (2001, $\alpha_\nu = 0.44$). We obtained R = 337 ± 10 (Log(R) = 2.52). This value is in agreement with that of other peaked radio sources at z≥4.5, but also with the R of the high-z blazar[7] population (e.g., Belladitta et al. 2019). This may suggest that the non-thermal synchrotron emission of PSO J191+86 is Doppler boosted. Figure 8 shows the comparison between the radio luminosity at 8 GHz with the optical luminosity at 4400Å of PSO J191+86 and of all the RL QSOs discovered in the literature at similar redshift (z=4.5-5.5)[8]. From this figure it is clear that PSO J191+86 is one of the most luminous RL QSO at this redshift, confirming that the radio-emission is

---

[7] Blazars are RL AGN with the relativistic jets closely oriented to our line of sight (e.g., Urry & Padovani 1995).

[8] For these RL QSOs the luminosity at 8 GHz was computed starting from the observed flux at 1.4 GHz, and by assuming a radio spectral index of 0.75±0.25, as already done in other works (e.g., Bañados et al. 2015) since only few sources have a tabulated spectral index in the literature. However, the observed 1.4 GHz frequency corresponds to a rest-frame frequency of 7.7-9 GHz for z=4.5-5.5 sources, which is very close to 8 GHz. Therefore the lack of a measured spectral index has only a marginal impact on the computed radio luminosities. Instead the luminosity at 4400Å was computed from the de-reddened z_{PS1} band magnitude (the one available for all these sources) and assuming the optical spectral index of Vanden Berk et al. (2001, $\alpha_\nu = 0.44$).

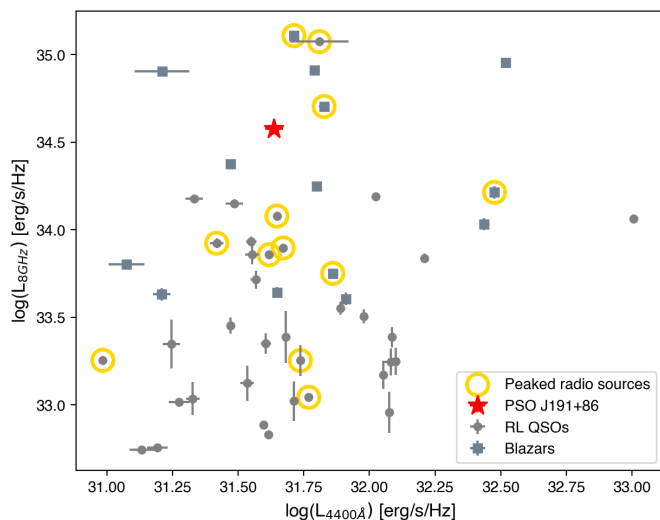produced in a powerful jet. A further investigation is necessary to properly interpret PSO J191+86 radio emission.

Fig. 8: Rest-frame radio luminosity at 8 GHz vs. the rest-frame optical luminosity at 4400Å for PSO J191+86 (red star) compared with z=4.5-5.5 radio-loud QSOs (grey points) discovered in the literature. Squares represent all the sources defined as blazars in the literature on the basis of their radio and/or X–ray properties. Yellow circles represent all the sources identified as peaked spectrum objects in the literature (Coppejans et al. 2017; Shao et al. 2020, 2021). PSO J191+86 is one of the most luminous RL QSO at these redshifts, confirming the power of its radio emission.

7.3. X–ray emission

From the X–ray properties reported in Sect. 5 we computed an X–ray luminosity of $5.33^{+1.54}_{-1.31} \times 10^{45}$ erg s^{-1} in the [2-10] keV energy band[9]. This value clearly asseses that the X–ray emission of PSO J191+86 largely overwhelms that expected from a typical hot X–ray corona and, hence, originates in a powerful jet. This is particular evident when plotting the SED of PSO J191+86 (Fig. 9): the X–ray emission is flatter and stronger with respect to that of RQ AGN with the same optical luminosity, according to the L_X-L_{UV} relation of Just et al. (2007).

The value of the photon index (Γ_X) computed from the *Swift – XRT* observation (Sect. 5) is flat (<1.5) in line with that of peaked radio sources (e.g., Snios et al. 2020) and blazars (e.g., Ighina et al. 2019) at high redshift. Therefore, we cannot exclude that the X–ray emission of PSO J191+86 is dominated by a relativistic jet oriented toward the Earth, as the high value of R suggests as well. This is also indicated by the value of the $\tilde{\alpha}_{\rm ox}$ of PSO J191+86, the ratio that quantify the relative strength of the X–ray emission with respect to the optical/UV component. The $\tilde{\alpha}_{\rm ox}$ is the two-point spectral index of a fictitious power law connecting 2500Å and 10 keV in the source rest frame (Ighina et al. 2019): $\tilde{\alpha}_{\rm ox} = -0.3026 \times \log(\frac{L_{10keV}}{L_{2500Å}})$. The value of the monochromatic luminosity at 10 keV rest frame has been computed from the observed flux density at [0.5-10] keV and by using the α_x

---

[9] $L_{02-10keV} = 4\pi D_L^2(1+z)^{\alpha_X-1}F[2-10 \text{ keV}]$, where z is the redsfhit estimated from the MgII line (see Table 5) and D_L the corresponding luminosity distance computed on https://www.astro.ucla.edu/~wright//CosmoCalc.html.

value[10]: $L_{10 keV} = 2.25^{+0.45}_{-0.41} \times 10^{27}$ erg s^{-1} Hz^{-1}. The luminosity at 2500Å instead has been measured from the flux density at 2500Å directly obtained from the LUCI 2 rest-frame spectrum: $L_{2500Å} = 5.56 \pm 0.40 \times 10^{31}$ erg s^{-1} Hz^{-1}. We found an $\tilde{\alpha}_{\rm ox}$ equal to $1.329^{+0.027}_{-0.025}$, which is similar to that of high-z blazars (e.g., Ighina et al. 2019).
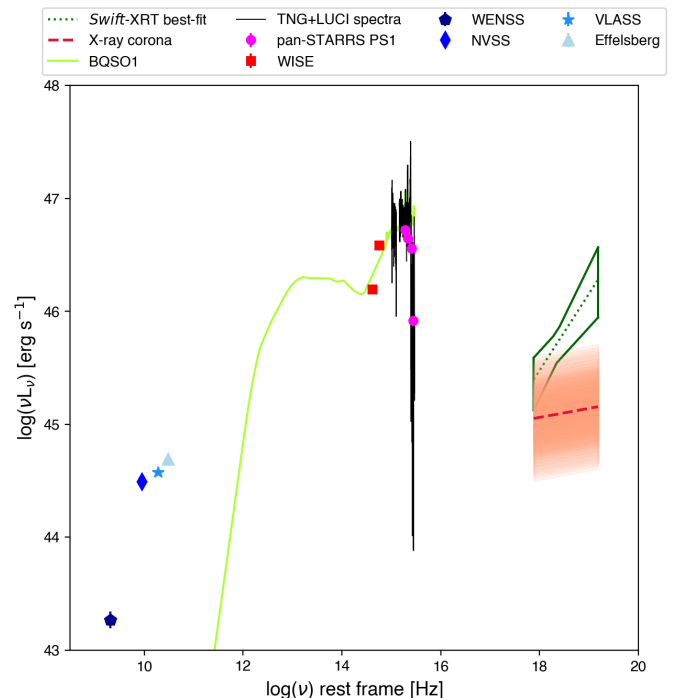

Fig. 9: Rest-frame SED of PSO J191+86 from radio to X–ray frequencies. In the X–ray we show the best fit emission in the observed [0.5-10] keV energy band (green dotted line) with its uncertainty. We also show the TNG and LUCI spectra (in black) and a quasar template (SWIRE template library; light-grey) as guide line. The red dashed line represents the coronal emission expected from a RQ AGN with the same $L_{2500Å}$ of PSO J191+86 according to the relation of Just et al. (2007), and the orange shaded area is the 1σ uncertainty on this estimate.

8. Discussion and conclusions

In this work we presented the discovery and multi-wavelength properties of PSO J191+86, a powerful radio QSO in the early Universe (z=5.32).

In the radio band, PSO J191+86 shows a possible peaked radio spectrum around ~1 GHz in the observed frame, corresponding to ~6.3 GHz in the rest frame. If this turnover will be confirmed, PSO J191+86 will be one of the powerful ($L_{1.4GHz} = 1.17 \times 10^{28}$ W Hz^{-1}) GPS source at z>5 ever discovered.

By assuming that the radio spectrum is peaked, we can compute the kinetic age of PSO J191+86 radio jets from the well-known correlation between peak frequency (ν_t in GHz) and projected angular size (l in kpc) derived by O'Dea & Baum 1997:

$$log(\nu_t) = -0.21(\pm 0.05) - 0.65(\pm 0.05)log(l) \quad (5)$$

Assuming that the peak of the spectrum is between 1 and 2 GHz (observed frame, i.e. ~6 and ~13 GHz in the rest-frame) we

---

[10] $L_{10keV} = \frac{L_{0.5-10keV}\nu_{10keV}^{(-\alpha_x+1)}}{(\nu_{10keV}^{-\alpha_x+1} - \nu_{0.5keV}^{-\alpha_x+1})}$

obtain l in the range ~10-30 pc (without taking into account the large scatter of the $\nu_t - l$ relation; e.g. Nyland et al. 2020). The corresponding kinetic age of the radio jets of PSO J191+86 would be in the range ~150-460 yr, by assuming a typical hot spot expansion velocity of 0.2c (e.g., Giroletti & Polatidis 2009; An & Baan 2012). This would make PSO J191+86 one of the youngest GPS source at z~5 ever discovered. Therefore, a detailed study of its radio emission could shed light on the triggering of radio activity in this distant QSO, on the formation and early stage evolution of its radio jets, on their interaction with the ambient medium and on their feedback on the host galaxy (e.g., Hardcastle & Croston 2020). However the non-simultaneity of the radio data in hand does not allow us to assess the real nature of the radio spectrum, because of possible variability. Simultaneous observations on a wide range of frequency are necessary to confirm the possible turnover.

The radio loudness of the source is very high (>300), making PSO J191+86 similar to the bulk population of blazars in the early Universe. Moreover the flat (Γ_X=1.32) and strong X–ray emission with respect to the optical one ($\tilde{\alpha_{ox}}$ = 1.329) are similar to those of blazars. Therefore PSO J191+86 could be a GPS object with the young relativistic jets oriented closely to our line of sight. This is not uncommon at high-z, since the blazar Q0906+6930 (Romani et al. 2004) at z=5.47 shows a clearly peaked radio spectrum (e.g., Coppejans et al. 2017; Mufakharov et al. 2020) with a turnover frequency of 6.4 GHz (observed frame), but, at the same time, Very Long Baseline Interferometry (VLBI) data found evidence of Doppler boosting (e.g., An. et al. 2020). These results suggest that J0906+6930 is a GPS source likely oriented towards the observer. Similarly a multifrequency VLBI follow-up for PSO J191+86 is in progress (Belladitta et al. in prep.) to spatially resolve the pc-scale radio emission of the source and to find evidence of Doppler boosting.

References

An, T., Mohan, P., Zhang, Y., et al. 2020, Nature Communications, 11, 143.
An, T. & Baan, W. A. 2012, ApJ, 760, 77.
Assef, R. J., Denney, K. D., Kochanek, C. S., et al. 2011, ApJ, 742, 93.
Astropy Collaboration, Price-Whelan, A. M., Sipőcz, B. M., et al. 2018, AJ, 156, 123.
Bañados, E., Venemans, B. P., Morganson, E., et al. 2015, ApJ, 804, 118.
Bañados, E., Venemans, B. P., Mazzucchelli, C., et al. 2018, Nature, 553, 473.
Bañados, E., Mazzucchelli, C., Momjian, E., et al. 2021, ApJ, 909, 80.
Belladitta, S., Moretti, A., Caccianiga, A., et al. 2019, A&A, 629, A68.
Belladitta, S., Moretti, A., Caccianiga, A., et al. 2020, A&A, 635, L7.
Bisogni, S., di Serego Alighieri, S., Goldoni, P., et al. 2017, A&A, 603, A1.
Blandford, R., Meier, D., & Readhead, A. 2019, ARA&A, 57, 467.
Caccianiga, A., Moretti, A., Belladitta, S., et al. 2019, MNRAS, 484, 204.
Carnall, A. C., Shanks, T., Chehade, B., et al. 2015, MNRAS, 451, L16.
Chambers, K. C., Magnier, E. A., Metcalfe, N., et al. 2016, arXiv:1612.05560
Coatman, L., Hewett, P. C., Banerji, M., et al. 2017, MNRAS, 465, 2120.
Condon, J. J., Cotton, W. D., Greisen, E. W., et al. 1998, AJ, 115, 1693.
Coppejans, R., van Velzen, S., Intema, H. T., et al. 2017, MNRAS, 467, 2039.
Corbin, M. R. & Boroson, T. A. 1996, ApJS, 107, 69.
Cutri, R. M., Wright, E. L., Conrow, T., et al. 2012, Explanatory Supplement to the WISE All-Sky Data Release Products
Dalla Bontà, E., Peterson, B. M., Bentz, M. C., et al. 2020, ApJ, 903, 112.
Dallacasa, D., Stanghellini, C., Centonza, M., et al. 2000, A&A, 363, 887
De Rosa, G., Venemans, B. P., Decarli, R., et al. 2014, ApJ, 790, 145.
Diamond-Stanic, A. M., Fan, X., Brandt, W. N., et al. 2009, ApJ, 699, 782.
Diana, A., Caccianiga, A., Ighina, L., et al. 2022, MNRAS, 511, 5436.
Evans, P. A., Beardmore, A. P., Page, K. L., et al. 2009, MNRAS, 397, 1177.
Fabian, A. C. 2012, ARA&A, 50, 455.
Farina, E. P., Schindler, J.-T., Walter, F., et al. 2022, arXiv:2207.05113
Fitzpatrick, E. L. 1999, PASP, 111, 63.
Gargiulo, A., Fumana, M., Bisogni, S., et al. 2022, MNRAS, 514, 2902.
Gaskell, C. M. 1982, ApJ, 263, 79.
Giroletti, M. & Polatidis, A. 2009, Astronomische Nachrichten, 330, 193.
Greene, J. E., Peng, C. Y., & Ludwig, R. R. 2010, ApJ, 709, 937.
Hardcastle, M. J. & Croston, J. H. 2020, New A Rev., 88, 101539.
Healey, S. E., Fuhrmann, L., Taylor, G. B., et al. 2009, AJ, 138, 1032.
Ighina, L., Caccianiga, A., Moretti, A., et al. 2019, MNRAS, 489, 2732.
Intema, H. T., Jagannathan, P., Mooley, K. P., et al. 2017, A&A, 598, A78.
Just, D. W., Brandt, W. N., Shemmer, O., et al. 2007, ApJ, 665, 1004.
Kalberla, P. M. W., Burton, W. B., Hartmann, D., et al. 2005, A&A, 440, 775.
Karouzos, M., Woo, J.-H., Matsuoka, K., et al. 2015, ApJ, 815, 128.
Kellermann, K. I., Sramek, R., Schmidt, M., et al. 1989, AJ, 98, 1195.
Lacy, M., Baum, S. A., Chandler, C. J., et al. 2020, PASP, 132, 035001.
Liu, Y., Wang, R., Momjian, E., et al. 2021, ApJ, 908, 124.
Mainzer, A., Bauer, J., Grav, T., et al. 2011, ApJ, 731, 53.
Marziani, P., Sulentic, J. W., Dultzin-Hacyan, D., et al. 1996, ApJS, 104, 37.
Marziani, P., Sulentic, J. W., Negrete, C. A., et al. 2010, MNRAS, 409, 1033.
Marziani, P., Sulentic, J. W., Plauchu-Frayn, I., et al. 2013, A&A, 555, A89.
Marziani, P., del Olmo, A., Martínez-Carballo, M. A., et al. 2019, A&A, 627, A88.
Massaro, F., Giroletti, M., D'Abrusco, R., et al. 2014, ApJS, 213, 3.
Mazzucchelli, C., Bañados, E., Venemans, B. P., et al. 2017, ApJ, 849, 91.
McGreer, I. D., Becker, R. H., Helfand, D. J., et al. 2006, ApJ, 652, 157.
McLure, R. J. & Dunlop, J. S. 2004, MNRAS, 352, 1390.
McMullin, J. P., Waters, B., Schiebel, D., et al. 2007, Astronomical Data Analysis Software and Systems XVI, 376, 127
Mufakharov, T., Mikhailov, A., Sotnikova, Y., et al. 2021, MNRAS, 503, 4662.
Nyland, K., Dong, D. Z., Patil, P., et al. 2020, ApJ, 905, 74.
O'Dea, C. P. & Baum, S. A. 1997, AJ, 113, 148.
O'Dea, C. P. & Saikia, D. J. 2021, A&A Rev., 29, 3.
Oke, J. B. 1990, AJ, 99, 1621.
Onoue, M., Bañados, E., Mazzucchelli, C., et al. 2020, ApJ, 898, 105.
Orienti, M. & Dallacasa, D. 2020, MNRAS, 499, 1340.
Padovani, P., Alexander, D. M., Assef, R. J., et al. 2017, A&A Rev., 25, 2.
Raiteri, C. M., Acosta Pulido, J. A., Villata, M., et al. 2020, MNRAS, 493, 2793.
Rakshit, S., Stalin, C. S., & Kotilainen, J. 2020, ApJS, 249, 17.
Rengelink, R. B., Tang, Y., de Bruyn, A. G., et al. 1997, A&AS, 124, 259.
Richards, G. T., Kruczek, N. E., Gallagher, S. C., et al. 2011, AJ, 141, 167.
Romani, R. W., Sowards-Emmerd, D., Greenhill, L., et al. 2004, ApJ, 610, L9.
Runnoe, J. C., Brotherton, M. S., DiPompeo, M. A., et al. 2014, MNRAS, 438, 3263.
Sbarrato, T., Ghisellini, G., Nardini, M., et al. 2012, MNRAS, 426, L91.
Schindler, J.-T., Farina, E. P., Bañados, E., et al. 2020, ApJ, 905, 51.
Seifert, W., Appenzeller, I., Baumeister, H., et al. 2003, Proc. SPIE, 4841, 962.
Shao, Y., Wagg, J., Wang, R., et al. 2020, A&A, 641, A85.
Shao, Y., Wagg, J., Wang, R., et al. 2021, arXiv:2112.03133
Shen, Y., Greene, J. E., Strauss, M. A., et al. 2008, ApJ, 680, 169.
Shen, Y., Richards, G. T., Strauss, M. A., et al. 2011, ApJS, 194, 45.
Shen, Y. & Liu, X. 2012, ApJ, 753, 125.

Shen, Y., Wu, J., Jiang, L., et al. 2019, ApJ, 873, 35.
Snios, B., Siemiginowska, A., Sobolewska, M., et al. 2020, ApJ, 899, 127.
Sulentic, J. W., Bachev, R., Marziani, P., et al. 2007, ApJ, 666, 757.
Tang, B., Shang, Z., Gu, Q., et al. 2012, ApJS, 201, 38.
Tody, D. 1993, Astronomical Data Analysis Software and Systems II, 52, 173
Trakhtenbrot, B. & Netzer, H. 2012, MNRAS, 427, 3081.
Trakhtenbrot, B. 2021, Nuclear Activity in Galaxies Across Cosmic Time, 356, 261.
Urry, C. M. & Padovani, P. 1995, PASP, 107, 803.
Vanden Berk, D. E., Richards, G. T., Bauer, A., et al. 2001, AJ, 122, 549.
Vestergaard, M. & Wilkes, B. J. 2001, ApJS, 134, 1.
Vestergaard, M. 2002, ApJ, 571, 733.
Vestergaard, M. & Peterson, B. M. 2006, ApJ, 641, 689.
Vestergaard, M. & Osmer, P. S. 2009, ApJ, 699, 800.
Vietri, G., Piconcelli, E., Bischetti, M., et al. 2018, A&A, 617, A81.
Vito, F., Mignoli, M., Gilli, R., et al. 2022, A&A, 663, A159.
Volonteri, M., Silk, J., & Dubus, G. 2015, ApJ, 804, 148.
Wills, B. J., Brotherton, M. S., Fang, D., et al. 1993, ApJ, 415, 563.
Wright, E. L., Eisenhardt, P. R. M., Mainzer, A. K., et al. 2010, AJ, 140, 1868.
Yi, W.-M., Wang, F., Wu, X.-B., et al. 2014, ApJ, 795, L29.
Zeimann, G. R., White, R. L., Becker, R. H., et al. 2011, ApJ, 736, 57.
Zuo, W., Wu, X.-B., Fan, X., et al. 2020, ApJ, 896, 40.